Multiple-image radiography

Miles N. Wernick,[1,5] Oliver Wirjadi,[2,7] Dean Chapman,[3,8] Zhong Zhong,[4] Nikolas P. Galatsanos,[2,9] Yongyi Yang,[2] Jovan G. Brankov,[2] Oral Oltulu,[3,10] Mark A. Anastasio,[5] and Carol Muehleman[6]

[1] Corresponding author. Department of Electrical and Computer Engineering, Illinois Institute of Technology, 3301 South Dearborn Street, Chicago, IL 60616, USA. e-mail: wernick@iit.edu phone: +1 312.567.8818.

[2] Department of Electrical and Computer Engineering, Illinois Institute of Technology, Chicago, IL 60616, USA

[3] Department of Physics, Illinois Institute of Technology, Chicago, IL 60616, USA

[4] National Synchrotron Light Source, Brookhaven National Laboratory, Upton, NY 11973, USA

[5] Department of Biomedical Engineering, Illinois Institute of Technology, Chicago, IL 60616, USA

[6] Department of Anatomy and Cell Biology, Rush Medical College, Chicago, IL 60612, USA

7 Visiting from Technische Universität Berlin, Berlin, Germany

8 Present address: Department of Anatomy and Cell Biology, College of Medicine, A315 Life Sciences Building, 107 Wiggins Road, Saskatoon, SK, S7N 5E5, Canada

9 Present address: Department of Computer Science, University of Ioannina, P.O. Box 1186 – GR 45110, Ioannina, Greece

10 Present address: Harran University, Department of Physics, Sanliurfa, Turkey 63300

Abstract

Conventional radiography produces a single image of an object by measuring the attenuation of an x-ray beam passing through it. When imaging weakly absorbing tissues, x-ray attenuation may be a suboptimal signature of disease-related information. In this paper we describe a new phase-sensitive imaging method, called multiple-image radiography (MIR), which is an improvement on a prior technique called diffraction-enhanced imaging (DEI). This paper elaborates on our initial presentation of the idea in [1]. MIR simultaneously produces several images from a set of measurements made with a single x-ray beam. Specifically, MIR yields three images depicting separately the effects of refraction, ultra-small-angle scatter, and attenuation by the object. All three images have good contrast, in part because they are virtually immune from degradation due to scatter at higher angles. MIR also yields a very comprehensive object description, consisting of the angular intensity spectrum of a transmitted x-ray beam at every image pixel, within a narrow angular range. Our experiments are based on data acquired using a synchrotron light source; however, in preparation for more-practical implementations using conventional x-ray sources, we develop and evaluate algorithms designed for Poisson noise, which is characteristic of photon-limited imaging. The results suggest that MIR is capable of operating at low photon count levels, therefore the method shows promise for use with conventional x-ray sources. The results also show that, in addition to producing new types of object descriptions, MIR produces substantially more-accurate images than its predecessor, DEI. MIR results are shown in the form of planar images of a phantom and a biological specimen. A preliminary demonstration of the use of MIR for computed tomography is also presented.

Introduction

Conventional radiography depicts only one object parameter—x-ray attenuation—neglecting other potentially informative effects of an object on the transmitted x-ray beam. In addition, conventional radiographs are degraded by the effect of scatter, which can significantly obscure image details.

Herein we present an x-ray imaging approach that produces a more-comprehensive description of the object, while rejecting virtually all undesired scatter. The images are obtained using a system of diffractive optical elements that allows the angular content of the beam to be analyzed. We refer to the method as *multiple-image radiography* (MIR), because it is based on computation of multiple parametric images of the object from multiple acquired images obtained using the crystal system. This paper elaborates on the initial presentation of the MIR technique given in [1].

MIR begins with computation of a relatively comprehensive object description in the form of an angular intensity spectrum of the transmitted beam, within a narrow angular range, for every image pixel. This is accomplished by applying a deconvolution step to the data obtained at every pixel. Next, the MIR method produces three parametric images—attenuation, refraction, and ultra-small-angle scatter—which are virtually immune to the undesired scatter that degrades conventional radiographs. Examples of these images are shown in **Figure 1**, along with a conventional radiograph of the same object for comparison. (Note that the radiograph shown in **Figure 1** was obtained using a synchrotron light source, so it shows somewhat better image quality than one would expect from a clinical radiography system.)

The MIR parametric images in **Figure 1** can be interpreted as follows. The MIR attenuation image (**Figure 1**, second image) is similar to a conventional radiograph, but exhibits much greater contrast owing to scatter rejection. The MIR refraction image (**Figure 1**, third image) depicts the effect of small beam deflections due to slowly varying refractive index variations in the object. The MIR ultra-small-angle scatter image (**Figure 1**, bottom image) quantifies angular divergence of the beam caused by the presence of textural structure within the object at a scale smaller than a pixel, but much larger than the x-ray wavelength. Paper fibers are a good example of such structure.

MIR is an improvement on a well-known previous technique called diffraction-enhanced imaging (DEI) [2]. The main advantages of MIR over DEI are: 1) MIR produces an ultra-small-angle scatter image, which DEI does not; 2) MIR corrects substantial errors inherent in DEI; and 3) MIR is more robust to noise than DEI.

Like DEI, MIR is expected initially to be best suited for applications involving small field-of-view imaging of soft tissue, such mammography and imaging of joints. DEI has already demonstrated a certain degree of success in both of these applications (e.g., [3],[4]), and we anticipate that MIR will enhance the results obtained by DEI while producing new information in the form of a scatter image.

The experiments reported in this paper are based on data acquired using a synchrotron light source. An aim of our research group is to produce a system, based on a small, conventional x-ray source, which can be used for clinical diagnostic purposes. Such a system is currently under development at the Illinois Institute of Technology. Because of the intensity limitations of conventional x-ray sources, we expect that this system will be photon-limited. Therefore, we assume in this paper that the acquired data

will be corrupted by Poisson noise, and we plan our algorithmic approaches accordingly. Specifically, we use iterative statistical methods (maximum-likelihood and Bayesian estimation), based on a Poisson linear model, to solve the required deconvolution problem.

In this paper, we concentrate on a planar-imaging mode, which we call MIR. However, we also show preliminary results in a computed-tomography mode, which we call MICT. Both sets of results show similar characteristics of the technique.

Because MIR can produce multiple images of the same object, MIR offers the possibility of segmenting the images into various tissue types by classifying the multivariate signature of each pixel. To illustrate this potential feature, we show preliminary image-segmentation results that capitalize on the multiple images produced by MIR.

In recent years, there has been increasing interest in x-ray imaging methods that derive contrast from the phase properties of the object [2,5-11]. The DEI method of Chapman *et al.* [2], precursor of the proposed MIR technique, is able to separate the effects of absorption and refraction by using two acquired images. Our research group has explored a curve-fitting method for determining fundamental beam parameters from x-ray images [12]. The contribution of MIR as compared with its predecessor, DEI, is that it produces ultra-small-angle scatter images, angular intensity spectra, more-accurate refraction and absorption images, and good noise performance from photon-limited data.

The rest of the paper is organized as follows. The following section explains the imaging model on which MIR is based, showing that the desired object information can be recovered from the measured data by deconvolution. Section 2 explains the

deconvolution algorithms, based on a Poisson-noise assumption, which we employed in our experiments. Parametric images derived from the deconvolved angular intensity spectra are defined in Section 3. We describe our experimental results in Sections 4 and 5, and provide a concluding discussion in Section 6.

1. MIR imaging model

To aid in the following discussion, let us first introduce spatial and angular coordinate systems as shown in Figure 2. We assume the beam is traveling along the *z*-axis.

In the proposed MIR method, data are acquired by illuminating the object with a collimated, monochromated x-ray beam and measuring the transmitted radiation. In MIR, we focus our attention on transmitted beam components traveling at angles described by extremely small values of θ' (on the order of microradians) with respect to the optical axis of the imaging system.

To measure refraction and ultra-small-angle scatter, it is necessary to detect very small variations in the directionality of the transmitted beam. This is accomplished in the MIR method by using the same imaging system as DEI, which is shown in Figure 3. The first two crystals in the imaging system serve principally to collimate and monochromate the beam. After passing through the object, the transmitted beam is incident on a third crystal, called the *analyzer*, which reflects only those components of the beam traveling at or near the analyzer's Bragg angle θ_B, thus rejecting all components outside a narrow angular range. By rotating the analyzer, and acquiring multiple images along the way, it is possible to gain the information needed to compute the intensity and directionality

characteristics of the transmitted beam. The details of this computation are explained later in the paper.

MIR involves illuminating the object with an x-ray beam of significant spatial extent (ideally covering the entire region of interest of the object). However, because the crystal optics reject angular components of the beam that are outside a narrow range, the imaging process can be viewed as essentially a pixel-by-pixel operation, with little or no crosstalk between adjacent pixels. The issue of crosstalk is further discussed in Appendix A.

Let us consider the portion of the beam destined for a particular pixel. The object will influence this portion of the beam by attenuating it (by absorption and scatter rejection), deflecting it (by refraction), and increasing its angular divergence (by ultra-small-angle scatter). These effects are all captured by the input-output relationship between the angular intensity spectrum of the illuminating beam and that of the transmitted beam.

Because the analyzer crystal is insensitive to intensity variations in the ϕ direction, we will simplify the notation by suppressing the ϕ-dependence of the angular intensity spectra. We will also assume for notational simplicity that the initial beam is spatially uniform within the region of interest.

1.1 Measurements with object absent

To understand the relationship between the input and output angular intensity spectra, let us develop a model of the measured intensity. When no object is present in the beam, the total intensity at the detector plane as a function of analyzer setting θ is given by

$$g(\theta; x, y) = \int_{-\infty}^{\infty} I_0(\theta') R_1(\theta') R_2(\theta') R_A(\theta - \theta') d\theta' \triangleq R(\theta), \quad (1)$$

where $I_0(\theta)$ represents the angular spectrum of the initial beam; $R_1(\theta)$, $R_2(\theta)$, and $R_A(\theta)$ denote the intensity reflectivity functions of the two monochromator crystals and the analyzer crystal, respectively. The integration over θ' describes the action of the detector, which is insensitive to angle. Equation (1) is based on a well-known geometrical-optics approximation of the interaction of the beam with the crystals [13].

The function $R(\theta)$ defined in equation (1) is known as the *intrinsic rocking curve*, because it is an intrinsic property of the imaging system, representing the intensity measured at the detector when the analyzer crystal is "rocked" (rotated in angle θ) when no object is present. The intrinsic rocking curve is assumed to be known, because it is easily measured.

Equation (1) has the simple form of a convolution, and can be written more compactly as

$$R(\theta) = I_0'(\theta) * R_A(\theta), \quad (2)$$

where $*$ denotes convolution and

$$I_0'(\theta) = I_0(\theta) R_1(\theta) R_2(\theta) \quad (3)$$

represents the angular intensity spectrum of the beam that illuminates the object (after preparation by the monochromator).

1.2 Measurements with object present

Using the same assumptions as transport theory [14], we will treat beam propagation through the object as linear in intensity; therefore, the effect of the object on the beam can be regarded as a linear system in terms of the angle θ. Thus, the angular intensity

spectrum of the beam after passing through the object (but before diffracting from the analyzer) can be described by:

$$I(\theta;x,y)=\int_{-\infty}^{\infty} I_0'(\theta')f(\theta,\theta';x,y)d\theta', \tag{4}$$

where the function $f(\theta,\theta';x,y)$ is the impulse response of the object. Physically, $f(\theta,\theta';x,y)$ represents the angular intensity spectrum of the transmitted beam that would be measured if the object were illuminated with a perfectly collimated beam, i.e., a beam having angular intensity spectrum $I_0'(\theta)=I_0\delta(\theta)$.

We will also assume that, within the ultra-small-angle regime in which the measurements are taken, the angular intensity pattern caused by sub-pixel object structures is nearly invariant to θ. In other words, we assume that the shape (but not the direction) of the angular pattern is unchanged by reorienting the illuminating beam by an angle on the order of microradians.

Under this assumption of angle-invariance, the effect of the object on the beam's angular intensity spectrum (equation (4)) reduces simply to the following convolution:

$$I(\theta)=\int_{-\infty}^{\infty} I_0'(\theta')f(\theta-\theta';x,y)d\theta'=I_0'(\theta)*f(\theta;x,y). \tag{5}$$

Thus, when the object is placed in the imaging system, the measured angular intensity spectrum becomes

$$g(\theta;x,y)=I_0'(\theta)*f(\theta;x,y)*R_A(\theta). \tag{6}$$

Commuting the convolutions, grouping terms, and using equation (2) we obtain:

$$g(\theta;x,y)=R(\theta)*f(\theta;x,y). \tag{7}$$

In practice, the image is sampled on a pixel grid, in which case equation (7) can be approximated in discrete form as:

$$g_{m,n}(\theta) = R(\theta) * f_{m,n}(\theta), \tag{8}$$

where (m,n) are discrete pixel indices. Equation (8) expresses a convolutional relationship between the measured intensities $g_{m,n}(\theta)$ and the impulse response $f_{m,n}(\theta)$. Within the limitations of the chosen imaging setup, the function $f_{m,n}(\theta)$ provides a rich description of the object's effect on the beam. This function will form the basis of the remainder of the analyses in this paper.

The desired angular intensity spectrum $f_{m,n}(\theta)$ can be recovered from the observed intensity $g_{m,n}(\theta)$ by performing a deconvolution (inversion of equation (8)) at every spatial location (m,n). The following section explains the details of the deconvolution procedure.

2. Deconvolution of the angular intensity spectra

In practice, measurements of $g_{m,n}(\theta)$ are made at discrete rotational settings of the analyzer crystal, and the values thus obtained are represented using a grid of discrete pixels. We will enumerate the discrete analyzer settings by index $k = 1,\ldots,K$, and the pixels by discrete spatial indices $m = 1,\ldots,M$, $n = 1,\ldots,N$ Thus, the desired function $f_{m,n}(\theta)$ that describes the object is replaced in the following discussion by the discrete quantity $f_{m,n}[k]$, $R(\theta)$ is replaced by $R[k]$, and the observed intensities $g_{m,n}(\theta)$ become $g_{m,n}[k]$.

In each of the deconvolution methods described below, we assume the data to be photon-limited, so that Poisson noise is the dominant noise source. Thus, our observation model is as follows:

$$g_{m,n}[k] \sim Poisson\left(R[k] * f_{m,n}[k]\right). \tag{9}$$

The aim of the following methods is to invert this model to estimate $f_{m,n}[k]$; the differences among the methods lie in the way in which they aim to lessen the effect of noise.

In the following sections, to simplify notation, we will sometimes represent images as vectors (indicated by bold letters). For example, $\mathbf{f}_{m,n}$ will denote the discrete angular intensity spectrum at an individual pixel (m,n), and $\mathbf{f}$ will denote a one-dimensional (vector) representation of the three-dimensional function $f_{m,n}[k]$ obtained by lexicographic ordering of the pixel values.

2.1 Maximum-likelihood (ML) solutions

The maximum-likelihood (ML) solution of the deconvolution problem is the value of $\mathbf{f}_{m,n}$ that maximizes the Poisson likelihood function for each pixel, i.e.,

$$\hat{\mathbf{f}}_{m,n} = \arg\max_{\mathbf{f}_{m,n}} p(\mathbf{g};\mathbf{f}_{m,n}), \quad m = 1,\ldots,M,\ n = 1,\ldots,N\ , \tag{10}$$

where

$$p(\mathbf{g};\mathbf{f}_{m,n}) = \prod \frac{\left(R[k] * f_{m,n}[k]\right)^{g_{m,n}[k]}\, e^{-R[k]*f_{m,n}[k]}}{g_{m,n}[k]!}\ . \tag{11}$$

A constrained solution of equations (10) and (11) can be obtained by using the well-known expectation-maximization (EM) algorithm [15]. The EM algorithm for this deconvolution problem produces a solution that is guaranteed to be non-negative if the initial estimate is non-negative. The iteration, which is widely used in nuclear-medicine imaging [16], is described by the following expression:

$$\hat{f}_{m,n}^{(i+1)}[k] = \frac{\hat{f}_{m,n}^{(i)}[k]}{\sum_{k+1}^{K} R[k]} \left\{ R[k] \star \left[\frac{g_{m,n}[k]}{R[k] * \hat{f}_{m,n}^{(i)}[k]} \right] \right\} , \tag{12}$$

where $\hat{f}_{m,n}^{(i)}[k]$ denotes the *i*th estimate of $f_{m,n}[k]$, and ★ denotes cross correlation. Note that the iterative deconvolution in equation (12) is performed separately at each pixel because the likelihood functions are not coupled in any way. Also note that, since the rocking curve is even, the cross correlation in equation (12) can be replaced by convolution.

In practice, if the noise level is high, this algorithm is usually stopped prematurely to stabilize the solution in the presence of noise. Early stopping of the EM algorithm amounts to an implicit method of regularization.

2.2 Maximum a posteriori (MAP) solution

When there is an appreciable amount of noise in the data, an explicit regularization approach may be preferred. In this study, we employed a Bayesian approach based on the maximum *a posteriori* (MAP) criterion, i.e.,

$$\hat{\mathbf{f}}_{m,n} = \arg\max_{\mathbf{f}_{m,n}} p(\mathbf{f}_{m,n}; \mathbf{g}), \quad m = 1,\ldots,M, \, n = 1,\ldots,N \ , \tag{13}$$

where $p(\mathbf{f})$ represents a prior probability law on $\mathbf{f}$ that reflects known properties of the actual signal, and $p(\mathbf{g};\mathbf{f}_{m,n})$ has the same form as the likelihood function in equation (11) . In the present context, the prior informs the algorithm that we expect the angular intensity spectrum to be a smooth function.

In our studies, we represent this knowledge by way of a Gibbs prior, which has the following form:

$$p(\mathbf{f}) = \frac{1}{Z}\exp\left(-\beta\sum_{l} V_l(\mathbf{f})\right), \tag{14}$$

in which the potential functions $V_k(\mathbf{f})$ are defined so that smoother functions are favored over less-smooth ones, β controls the strength of the prior, Z is a normalizing constant, and the summation is over sets of pixels called cliques. Adoption of a Gibbs prior is equivalent to an assumption that $\mathbf{f}$ is a Markov random field [17].

A modified EM algorithm [18] can be used to find the MAP solution. The general form of the iterative procedure is:

$$\hat{f}_{m,n}^{(i+1)}[k] = \frac{\hat{f}_{m,n}^{(i)}[k]}{\sum_{k=1}^{K} R[k] + \beta\dfrac{\partial V(\mathbf{f})}{\partial f_{m,n}[k]}}\left\{R[k]\star\left[\frac{g_{m,n}[k]}{R[k] * \hat{f}_{m,n}^{(i)}[k]}\right]\right\} \tag{15}$$

wherein the derivative term in the denominator depends on the specific choice of the prior.

In the following we describe two ways to define the prior, and thus two specific choices for the derivative term. Specifically, we can choose to impose smoothness only along the k-axis of the discretized angular intensity spectrum, thus encouraging each pixel's angular intensity spectrum to be a smooth function. Alternatively, we can impose smoothness spatially as well, thus utilizing the knowledge that, because of their close proximity, neighboring pixels will tend to have similar angular intensity spectra. Following nomenclature from the image-processing field [19], we describe each pixel's angular intensity spectrum as a *channel*; thus, we describe the former approach as a *single-channel* method, and the latter as a *multichannel* method.

2.2.1 *Single-channel MAP solution.* In a single-channel solution, we impose smoothness only along the k-axis of each *angular intensity spectrum*; thus the deconvolution procedure for each pixel is performed independently of all the others, just as in the ML approach. In this case, the potential functions are as follows:

$$V\left(f_{n,m}[k]\right) = \sum_{i=1}^{K}\left\{\left[2f_{n,m}[i] - f_{n,m}[i-1] - f_{n,m}[i+1]\right]^2\right\}. \tag{16}$$

This has the effect of penalizing large variations in values along the k-axis of the angular intensity spectrum at each pixel.

2.2.2 *Multichannel MAP solution* In the multichannel solution, we assume additionally that the images are spatially smooth. This assumption is reflected in the following potential function:

$$V\left(f_{n,m}[k]\right) = \sum_{i=1}^{K}\left\{\begin{array}{l}\left[2f_{n,m}[i] - f_{n,m}[i-1] - f_{n,m}[i+1]\right]^2 \\ +\left[4f_{n,m}[i] - f_{n-1,m}[i] - f_{n,m-1}[i] - f_{n+1,m}[i] - f_{n,m+1}[i]\right]^2\end{array}\right\}, \tag{17}$$

which penalizes large variations among immediate spatial and angular neighbors in the function $f_{m,n}[k]$, with neighborhoods defined as shown in Figure 4.

3. Computation of parametric images

The angular intensity spectrum $f_{m,n}[k]$ is a three-dimensional image, with two spatial dimensions and one angular dimension. The function $f_{m,n}[k]$ is a rich source of information about the object, but can be made easier to interpret by distilling it into a small number of two-dimensional parametric images for visualization purposes.

In our experiments, we summarize the angular intensity spectrum at each pixel by three values, representing attenuation, refraction, and ultra-small-angle scatter. Thus, we

obtain three images of any given object. In Appendix B we show that each of the three parametric images we propose can be expressed as a property that is either exactly linear or nearly linear with object thickness. This property is important both for image interpretation and to enable computed tomography (CT) reconstruction by conventional methods.

The computed parametric images are specified in the definitions that follow. These definitions are stated in terms of the following quantities: the total intensity at a given pixel (m,n),

$$T_{m,n} = \sum_{k=1}^{K} \hat{f}_{m,n}[k]; \tag{18}$$

the angular intensity spectrum at this pixel normalized by its total intensity,

$$F_{m,n}[k] = \frac{\hat{f}_{m,n}[k]}{T_{m,n}}; \tag{19}$$

the total intensity at each pixel in the absence of the object,

$$I_0 = \sum_{k=1}^{K} R[k];$$

and the angular spacing $\Delta\theta$ of the samples in $f_{m,n}[k]$.

3.1.1 *Attenuation image.* In the ultra-small-angle regime, attenuation of the x-ray beam is caused both by absorption and by scattering into angles outside the measured range. These sources of beam attenuation are collectively summarized by the following parameter:

$$a_{m,n} = -\ln T_{m,n}[k], \tag{20}$$

which is simply a discrete inversion of an exponential loss law. This image conveys the same information as a conventional radiograph or DEI absorption image aims to convey; however, it produces a much more accurate result than either of these methods, as we will show later.

3.1.2 *Refraction image.* Refraction induces an overall deflection of the beam, which we measure as the angular shift of the beam centroid (as compared to its position when no object is present), i.e.,

$$r_{m,n} = \left(\sum_{k=1}^{K} k F_{m,n}[k] \right) \Delta\theta \,. \tag{21}$$

The angle $r_{m,n}$ is the same as that denoted by $\Delta\theta_Z$ in the original reference on DEI [2]; however, as we will see later, the values of this parameter can be computed much more accurately by MIR than by DEI.

3.1.3 *Ultra-small-angle scatter image.* Ultra-small-angle scatter by sub-pixel object structures causes angular broadening of the beam. We characterize this broadening by the beam's angular divergence about the angle $r_{m,n}$, as measured by the second central moment of the normalized angular intensity spectrum, i.e.,

$$s_{m,n} = \sum_{k=1}^{K} (k\Delta\theta - r_{m,n})^2 F_{m,n}[k]. \tag{22}$$

This quantity is simply the variance of the net random deflection angle of individual photons.

4. Experiment 1: MIR projection imaging of a phantom

4.1 Phantom and data collection

A physical phantom was constructed (**Figure 5**), which exhibits various combinations of refraction, absorption, and scattering effects. Staggered sheets of paper were arranged so that the number of layers of paper ranged from one to eight. A cylindrical Lucite rod (radius 6 mm, length 51mm) was placed in front of the paper. The paper in the phantom is expected to produce ultra-small-angle scattering, but little refraction; the converse is true for Lucite. The entire phantom was in contact with a sheet of Lucite (6.35 mm thickness). A steel ball used for alignment appears in the corner.

The phantom was imaged using 18keV x-rays at the National Synchrotron Light Source X15A imaging beamline. A total of 24 images of the phantom were acquired at 0.8 μradian increments from –9.6 to +8.8 μradians. The photon flux incident on the object was approximately 5.3×10^6 ph/mm^2 (1.1 mGy absorbed surface dose in water). Each image consisted of 1256×444 pixels of dimension 50 μm $\times$ 50 μm. The detector was an x-ray photostimulable image plate (Fuji HR-V image plate, Fuji BAS-2500 reader with 50 μm $\times$ 50 μm pixel size). Background and scattered radiation on the image plate were reduced by slits. The remaining background was subtracted from every pixel in each image.

4.2 Simulation of photon-limited data

A clinical MIR imaging device under development will most likely be photon-limited; therefore, we investigated the effect of Poisson noise on the results of our deconvolution methods. As a basis for simulating the effect of a photon-limited imaging

environment, we considered the acquired synchrotron data to be approximately noise-free in comparison to the noise level we envision will prevail in a clinical device. Thus, we simulated the effect of photon noise by generating Poisson-distributed image values in software based on the "noise-free" acquired data. In this experiment, we quantify the noise level by the highest mean photon count per pixel in the image.

We created simulated data sets for two cases: 300 ph/pixel and 50 ph/pixel. Assuming the pixel size to be 50 μm × 50 μm, these photon counts correspond to 25 μGy and 4.2 μGy, respectively (surface dose absorbed in water). In our simulation, we assumed the quantum efficiency of the detectors to be unity, which is reasonable at 18keV. Therefore, at 50 ph/pixel, the dose would be roughly equivalent to that of a typical diagnostic mammogram (40μGy) if images were acquired at 10 analyzer positions.

Phase contrast persists at high energies, therefore similar refraction and scatter images can be obtained at x-ray energy of 60keV, with the water-equivalent dose being reduced by a factor of about 7.

4.3 Experimental results

We found that the synchrotron data were best deconvolved using the EM algorithm (Section 2.1); the simulated, photon-limited data with a maximum of 300 ph/pixel were best processed with the single-channel MAP method (Section 2.2.1); and the data with a maximum of 50 ph/pixel were best analyzed using the multichannel MAP method (Section 2.2.2). This is not surprising since these methods are progressively more aggressive in their smoothing approach.

Examples of the deconvolved angular intensity spectra are shown in **Figure 6**. Each graph shows the angular intensity spectrum computed at one pixel in the image. At a pixel in the background, the deconvolved curve is a delta function (to within the smoothness imposed by the algorithm). Thus, in the background, the object's impulse response is itself an impulse function, meaning that the object has no refraction or scattering effect on the beam in background regions. At a pixel which lies off-center in the rod, the corresponding curve shows that the beam is deflected to the right by refraction, as expected. At a pixel where the rod and paper overlap, the curve shows that the beam is deflected by the rod, but also broadened by the paper. At a pixel where there is only paper, the associated curve shows that the beam is substantially broadened by ultra-small-angle scattering. In every pixel in the object, the beam is also attenuated.

Although the curves shown in **Figure 6** are clearly informative, the results are easier to interpret in the form of parametric images. **Figure 7** shows the results of parametric image computed at three noise levels: (a) "noise-free" image computed from the acquired synchrotron data; (b) maximum of 300 counts/pixel; and (c) maximum of 50 counts/pixel. The results show that, although image quality deteriorates somewhat with increasing noise level, the images are very informative even in the noisiest case.

The images shown exhibit expected characteristics of the object's effect on the beam. For example, the Lucite rod shows strong attenuation and refraction of the beam, but virtually no scattering. Also, predictably, the paper shows significant attenuation and very strong scattering, but only small refraction effects. Notably, the scatter produced by even one sheet of paper is clearly visible in the scatter image.

Noticeable scattering is also depicted at the edge of the rod; however, this is actually an artifact caused by partial volume effect (finite detector size). At these edge pixels, the rod occupies only a portion of these pixels; therefore, these pixels see a mixture of a highly refracted beam, and a beam that misses the rod entirely. The resulting bimodal angular intensity spectrum leads to a large value of the computed beam divergence. This artifact can be eliminated by an algorithm designed to detect such anomalous angular spectra; but, we did not investigate the issue further in this preliminary study, and we do not expect this effect to be so pronounced in biological specimens.

4.4 Comparison with DEI

The DEI method is based on a model that includes only attenuation and refraction effects (no scatter effects); thus, DEI produces highly erroneous results when ultra-small-angle scatter is present (which is virtually always the case in biological tissue). In addition, DEI uses a first-order Taylor-series approximation of the rocking curve, which in essence models the rocking curve as a triangular function. This approximation fails to utilize subtle features of the actual rocking curve, limits the range of refraction angles that can be measured, and can lead to sizeable errors in the images. These model assumptions would be expected to lead to significant inaccuracies in the results, and indeed they do.

Figure 8 shows that substantial errors can arise in the attenuation images produced by DEI, and that these are corrected by MIR. The plot in **Figure 8** shows the theoretical curve for attenuation by a rod, along with the experimental MIR and DEI results. MIR produces a close match, while DEI produces a significant distortion.

Figure 9 shows that substantial errors also exist in the refraction images obtained by DEI. One would expect the refraction image of the Lucite rod to be constant along the long axis of the rod. While this is roughly true of the MIR refraction image, the DEI refraction image exhibits a staircase profile, caused by contamination of the rod's refraction signal by the paper's scattering effect. Because MIR explicitly accounts for scatter, it produces an additional scatter image, and thus removes this contamination from the refraction image.

Figure 10 shows a comparison of DEI and MIR images computed from noisy data (maximum 50 ph/pixel). The MIR and DEI attenuation images appear comparable in their noise levels, but the DEI refraction image appears to have a substantially higher noise level than the corresponding MIR image. Further studies of noise performance will be performed as part of the effort to develop a compact MIR imaging system.

5. Experiment 2: MICT imaging

In the planar-imaging mode, the three MIR images can be expressed as line integrals of the absorption, refraction, and scatter properties, as explained in Appendix B. Thus, MIR data can be used to obtain computed tomography (CT) images by conventional linear reconstruction methods.

To demonstrate MIR in its computed tomography mode (MICT), we prepared a second phantom (**Figure 11**), consisting of a Lucite jar containing a Lucite rod and a sheet of paper rolled into a cylinder. The phantom was imaged using 40 keV x-rays at the National Synchrotron Light Source X15A imaging beamline. The object was rotated in 1-degree increments to obtain 360 projection images at each of 11 analyzer positions. The analyzer positions ranged from from –4 to +4 μradians with 0.8-microradian

increment. An exposure time of 0.5 second was used for each image. The photon flux rate incident on the object was approximately 5.3×10^6 ph/s/mm^2. Each image consisted of 1256×444 pixels of dimension 50 μm $\times$ 50 μm. For each projection, 20 images were taken without the object in the beam. The average of these images was used for normalization of the sample images to account for non-uniformity of the incident beam, which does not change with analyzer setting, or that introduced by the crystal optics, which does change with analyzer setting. In addition, 20 dark-current images were acquired and their average was subtracted from all images on a pixel-by-pixel basis before further processing. The detector was stationary during the imaging process, so an area of only 3 mm $\times$ 100 mm of the two-dimensional detector (RAD-ICON 2048) was used to acquire the images.

MIR projection images were computed from the data as in Experiment 1, and MICT images were reconstructed by conventional filtered backprojection (FBP) with a ramp filter.

The results, shown in **Figure 12**, exhibit the expected behavior in some ways, but not in others, suggesting that further theoretical developments will be needed to perfect the MICT method. As expected, the paper is represented by large values in the scatter image, and low values in the refraction image. Also expected is the strong refraction at the edges of the Lucite rod, and the constant attenuation within all the Lucite regions (jar and rod). However, unexpectedly, the paper roll exhibits high attenuation. We have not yet determined the cause of this apparent loss. In future studies, we plan to undertake a fully quantitative comparison of the results to theoretical predictions from scattering

theory. However, the results obtained to date are very encouraging that the subtle beam effects of refraction and scatter are clearly evident.

Figure 13 shows surface renderings of the paper and rod in the phantom, which were obtained by image segmentation. Because the paper and rod have different scatter and refraction properties, they are easily discriminated. This is a crude demonstration of the potential MIR has for characterization of materials and tissues.

6. Experiment 3: MIR imaging of a foot

To ensure that MIR performs as well in a realistic setting as in a simple phantom, we imaged an intact human foot. Data were acquired using 40 keV x-rays at five analyzer positions. The photon flux rate incident on the object was approximately 5.3×10^6 ph/s/mm^2. A skin dose of 0.12 mGy was delivered at each analyzer position.

Figure 14 shows attenuation, refraction, and ultra-small-angle scatter images of the foot specimen. Whereas conventional radiography shows only calcified tissue and, at low energies, shadows of soft tissue, MIR appears capable of depicting soft tissue detail such as tendons, connective tissue, and skin. Unfortunately, the clear depiction of cartilage, which has been reported for DEI [4], is not evident in these images because of the orientation of joint spaces with respect to the x-ray beam. However, many specific anatomical structures are evident in the refraction and scatter images, which are not normally visible in a conventional radiograph. For instance, although the two tendons on the dorsum of the foot consist of the same tissue type, they can easily be distinguished from one another in the refraction image due to refraction at their edges. The scatter image highlights the dense tissue on the heel of the foot and produces good image contrast the surface of the tendons.

The same images are shown in **Figure 15** in a color composite display, which suggests the potential of this technique for tissue characterization based on the multichannel nature of the images.

7. Conclusion

We have presented a method of imaging with x-rays that measures attenuation, refraction, and ultra-small-angle scatter of the beam, and can be performed in either planar-imaging or CT mode. We have developed a set of algorithms that perform well in the presence of Poisson noise, which will be needed for clinical imaging with a conventional x-ray source. In future work, we will describe our ongoing investigations of medical applications of the MIR technique, and we will validate the images quantitatively against predictions of wave propagation theory.

8. Appendix A: Magnitude of beam deflections in tissue

The MIR method assumes that the beam deflections due to refraction and scatter are too small to cause significant crosstalk between adjacent pixels. The DEI method makes the same assumption, but additionally assumes that there is no ultra-small-angle scatter is present at all.

Experimental evidence suggests that crosstalk is generally a small effect. Hasnah, *et al.*, [3] found experimentally that the refraction angle caused by a 1-cm thick slice of breast tissue was on the order of 0.001 to 0.01 μradians. Assuming the distance from the object to the detector to be 1m, this implies a spatial deflection on the detector face on the order of 0.001 to 0.01 μm. Thus, assuming 50-μm pixels, the beam deflection per

centimeter of breast tissue is expected to be about 1/5000 to 1/50000 of the width of a pixel.

In imaging an entire foot (**Figure 14**), we found the maximum refraction angle in the image to be 0.1 μradians (implying a deflection of 1/500 the width of a pixel). The standard deviation of the scatter-induced deflection for the pixel with the greatest scatter divergence was about 1.7 μradians (or 1/30 the width of a pixel).

9. Appendix B: Linearity of MIR object properties

If one is to employ linear CT reconstruction techniques, it is important that the MIR projection images behave linearly with object thickness. The linearity of the x-ray attenuation (extinction) coefficient is well-known [13], and the linearity of the refraction angle has been explained and demonstrated empirically in [20].

The MIR scatter parameter $s_{m,n}$ is not guaranteed theoretically to be linear in the most general circumstances, however it appears to be very nearly so in the proposed imaging situation. In this Appendix, we describe two cases in which linearity holds in theory, and we provide experimental evidence that linearity holds in practice based on a simple phantom.

First, according to transport theory, linearity of the angular divergence of the intensity spectrum holds if the scatterers in the material have Gaussian phase functions on average [14]. Although biological tissue contains a variety of scatterers, the MIR scatter image can be viewed as that of an equivalent object composed of Gaussian scatterers.

Second, linearity of the scatter parameter is a direct consequence of equation (5) (as is linearity of attenuation and refraction angle). To see this, let us suppose that the beam passes through two objects, one after the other, and let the impulse response

functions of these objects at a given (x, y) position be denoted by $f_1(\theta)$ and $f_2(\theta)$. By equation (5), the net impulse response of the two objects is $f(\theta) = f_1(\theta) * f_2(\theta)$. It is well known that the second central moment of the convolution of two functions is equal to the sum of the second central moments of the individual functions. This is the basis for the additivity of variances for independent random variables, and, indeed, the MIR scatter parameter can be viewed as the variance of the deflection angle of individual photons. Thus, the scatter parameter is a linear parameter under the convolutional model.

To test the linearity of the MIR scatter parameter, we performed a simple experiment using a phantom. A wedge-shaped Lucite container was filled with a suspension of polymethylmethacrylate (PMMA) microspheres in glycerine and imaged at at 18 keV. The mean diameter of the microspheres was 6.5 μm with standard deviation in the range of 3-10 μm. The volume density of the scatterers was 1.0×10^9 cm^{-3}. **Figure 16** shows empirical values of the scatter parameter $s_{m,n}$ as a function of sample thickness, along with a linear fit to the data. A least-squares fit to the data showed the relationship is linear at a significance level of $p < 10^{-4}$. These results suggest that a linear model for the MIR scatter parameter is a reasonable one, thus justifying the use of linear CT image reconstruction for MICT.

Acknowledgments

This research was supported by NIH/NIAMS grant AR48292 (M.N.W., D.C., Y.Y., J.G.B., C.M.), NIH/NIGMS grant GM59395 (O.O, D.C.), and U. S. Army MRMC grant DAMD17-99-9217 (D.C.). The National Synchrotron Light Source, Brookhaven National Laboratory, is supported by the U.S. Department of Energy, Division of Materials Sciences and Division of Chemical Sciences, Contract No. DE-AC02-

98CH10886 (Z.Z.). The authors thank Jun Li for his part in preparing and imaging the foot specimen, and Alejandro Saiz for his assistance in figure preparation. The authors also thank the anonymous reviewers for their helpful suggestions for improving the manuscript.

References

[1] M.N. Wernick, O. Wirjadi, D. Chapman, O. Oltulu, Z. Zhong, and Y. Yang, "Preliminary investigation of a multiple-image radiography method," *Proc. Intl. Symp. Biomed. Imaging*, pp. 129-132, 2002.

[2] D. Chapman, W. Thomlinson, R.E. Johnston, D. Washburn, E. Pisano, N. Gmür, Z. Zhong, R. Menk, F. Arfelli, D. Sayers, "Diffraction Enhanced X-ray Imaging", *Phys. Med. Biol*., vol. 42, pp. 2015-2025, 1997.

[3] M. O. Hasnah, et al., "Diffraction enhanced imaging contrast mechanisms in breast cancer specimens," *Med Phys*, vol. 29, pp. 2216-2221, 2002.

[4] J.A. Mollenhauer, et al, "Diffraction enhanced x-ray imaging of articular cartilage," *Osteoarthritis Cartilage*, vol. 10, pp. 163-171, 2002.

[5] R. Fitzgerald, "Phase-Sensitive X-ray Imaging," *Physics Today*, vol. 53 (7), 2000.

[6] K.M. Podurets, V.A. Somenkov, S.S. Shil'stein, "Refraction-contrast radiography," *Sov. Phys. Tech. Phys*., vol. 34, pp. 654-657, 1989.

[7] V.A. Somenkov, A.K. Tkalich, S.S. Shil'stein, "Refraction contrast in x-ray introscopy," *Sov. Phys. Tech. Phys*., vol. 36, pp. 1309-1311, 1991.

[8] V.N. Ingal, E.A. Beliaevsky, "X-ray plane wave topography observation of phase contrast from a non-crystalline object," *J. Phys.*, vol. 28, pp. 2314-2317, 1995.

[9] T.E. Gureyevand S.W. Wilkins, "Regimes of x-ray phase-contrast imaging with perfect crystals," *Il Nuovo Cimento*, vol. 19, pp. 545-552, 1997.

[10] D. Chapman, W. Thomlinson, Z. Zhong, R.E. Johnston, E. Pisano, D. Washburn, D. Sayers, C. Segre, "Diffraction enhanced imaging applied to materials science and medicine," *Synchrotron Radiation News*, vol. 11 (2), pp. 4-11, 1998.

[11] Z. Zhong, W. Thomlinson, D. Chapman, D. Sayers, "Implementation of diffraction enhanced imaging experiments at the NSLS and APS," *Nucl. Instrum. Meth. A*, vol. 450, pp. 556-567, 2000.

[12] O. Oltulu, Z. Zhong, M. Hasnah, M.N. Wernick, and D. Chapman, "Extraction of extinction, refraction and absorption properties in diffraction enhanced imaging," in review.

[13] J. Als-Nielsen and D. McMorrow, *Elements of Modern X-Ray Physics*, Wiley, 2001.

[14] A. Ishimaru, *Wave Propagation and Scattering in Random Media*, IEEE Press, 1997.

[15] A. P. Dempster, N. M. Laird, and D. B. Rubin, "Maximum likelihood from incomplete data via the EM algorithm," *J. Roy. Statist. Sect*., vol. 39, pp. 1-38, 1977.

[16] K. Lange and R. Carson, "EM reconstruction algorithms for emission and transmission tomography," *J. Comput. Assist. Tomog*., vol. 8, pp. 306-316, 1984.

[17] S. Geman and D. Geman. Stochastic relaxation, Gibbs distributions, and the Bayesian restoration of images. *IEEE Trans. on Patt. Anal. Machine Intell.*, 6(6):721-741, Nov. 1984.

[18] P. J. Green, "Bayesian reconstructions from emission tomography data using a modified EM algorithm," *IEEE Trans. Med. Imaging*, vol. 9, pp. 439-446, 1990.

[19] N. P. Galatsanos, M. N. Wernick, and A. K. Katsaggelos, "Multichannel Image Recovery," in *Handbook of Image and Video Processing*, A. Bovik, Ed., San Diego: Academic Press, pp. 155-168, 2000.

[20] F. A. Dilmanian, et al., "Computed tomography of x-ray index of refraction using the diffraction enhanced imaging method," *Phys. Med. Biol.*, vol. 45, pp. 933-946, 2000.

Figures

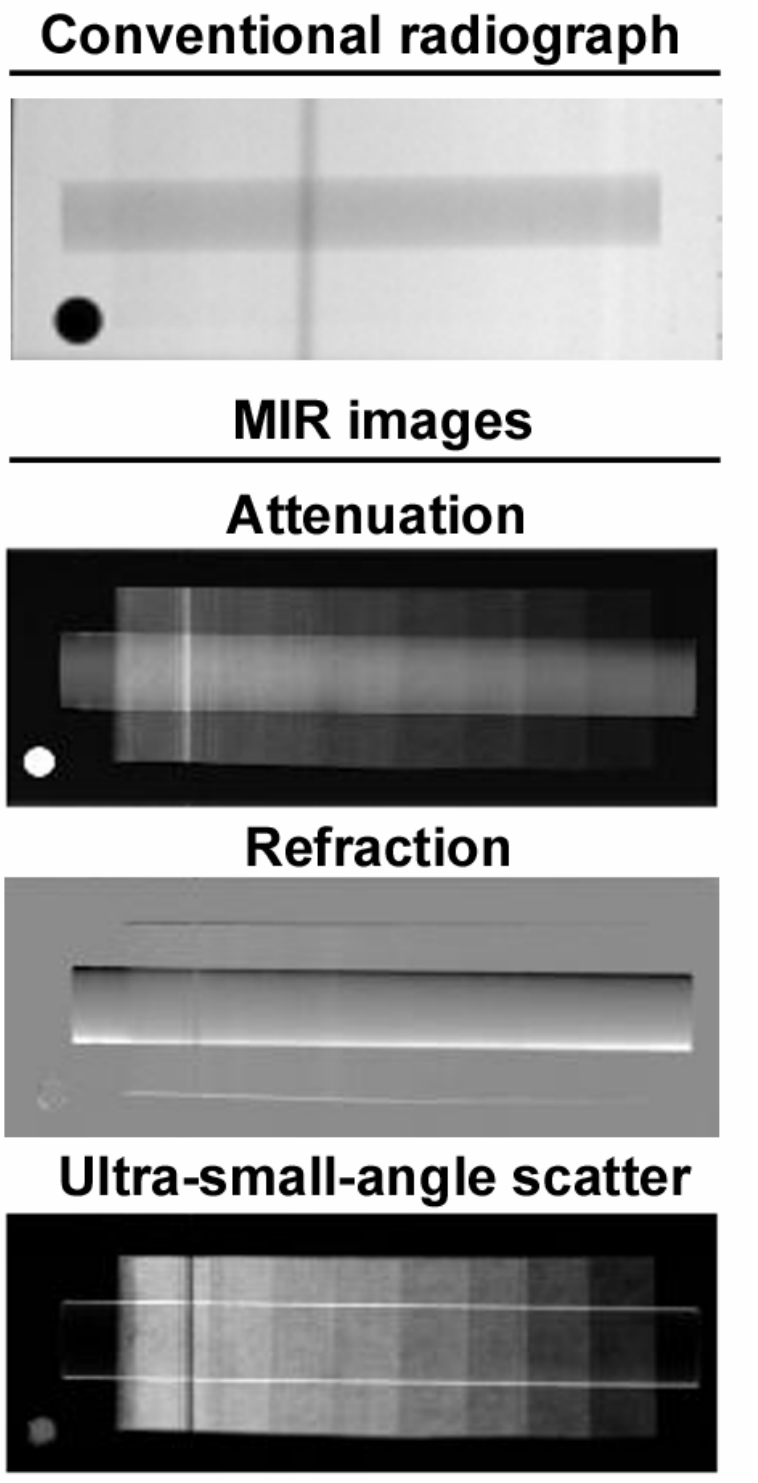

Figure 1. Examples of MIR projection images, along with conventional radiograph for comparison.

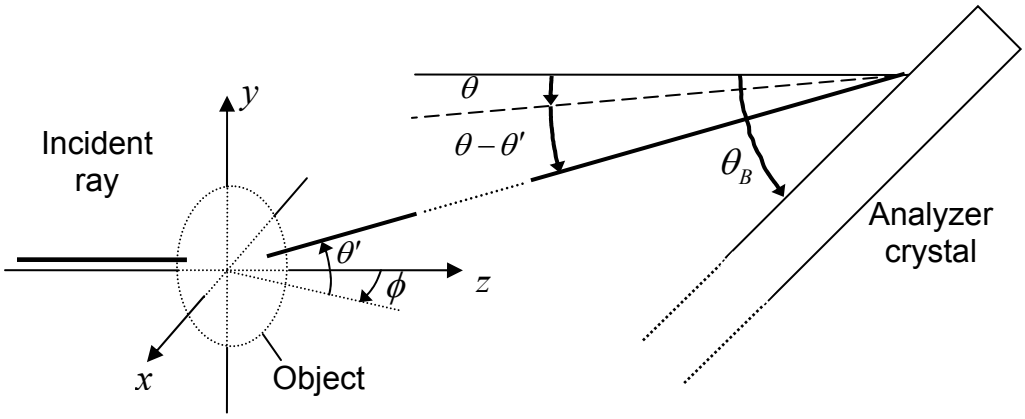

Figure 2. Definition of coordinate systems. Note that the figure is drawn out of proportion extremely for illustration purposes (in reality, all angles shown are on the order of microradians). Indicated in the figure are: angles θ and ϕ , which define the direction of a ray within the transmitted x-ray beam (describing refraction or ultra-small-angle scatter effects); the Bragg angle of the analyzer crystal θ_B; the angular setting of the analyzer θ_A; and the spatial coordinates (x, y, z).

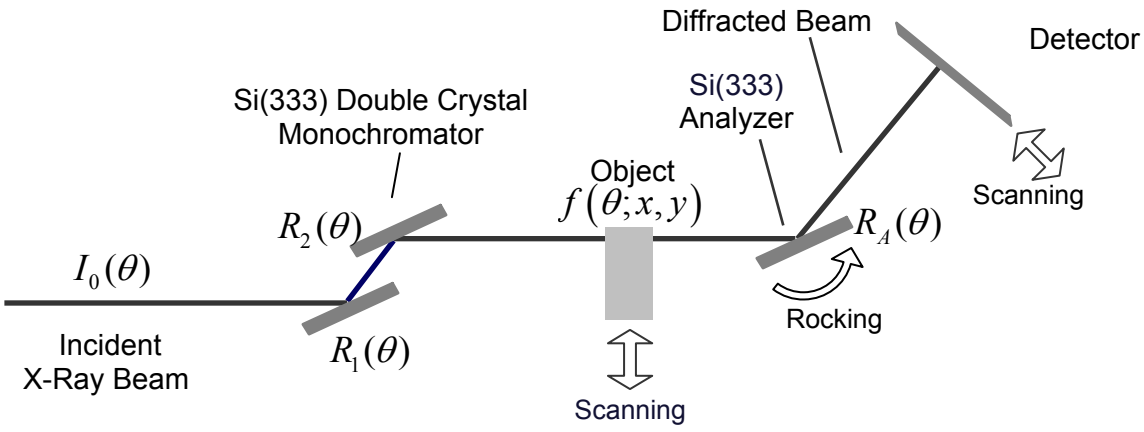

Figure 3. Schematic diagram of imaging system used in MIR. This is a well-known imaging configuration used commonly in phase-sensitive imaging. In MIR, the analyzer crystal is rotated (rocked) to make multiple measurements, from which the angular intensity spectrum of the beam is computed at each pixel.

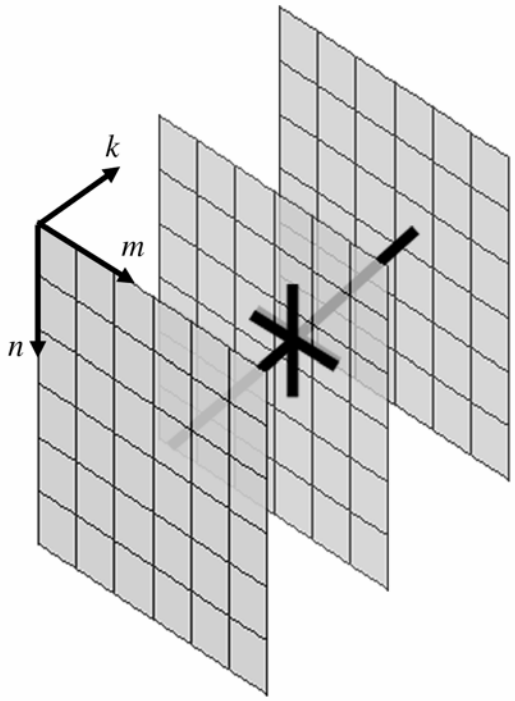

Figure 4. Neighborhood structure used in multichannel deconvolution method. Pixel values of the true angular intensity spectrum $f_{m,n}[k]$ are assumed correlated with values of pixels that are immediate spatial and angular neighbors.

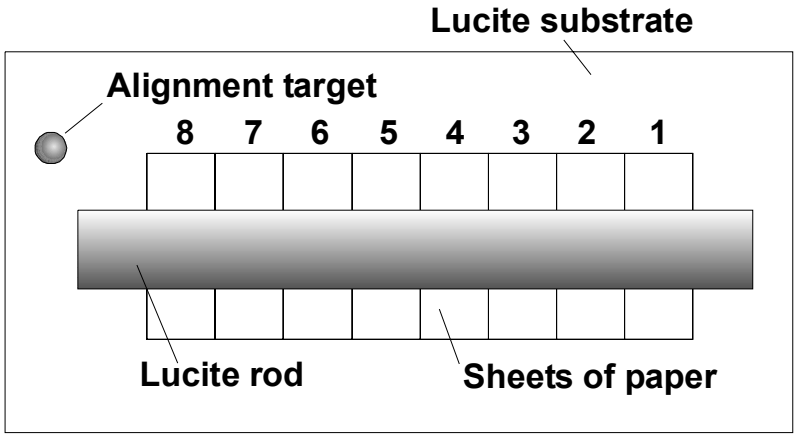

Figure 5. Phantom used in MIR projection-imaging study, consisting of a Lucite rod and layers of paper ranging from one to eight sheets in thickness.

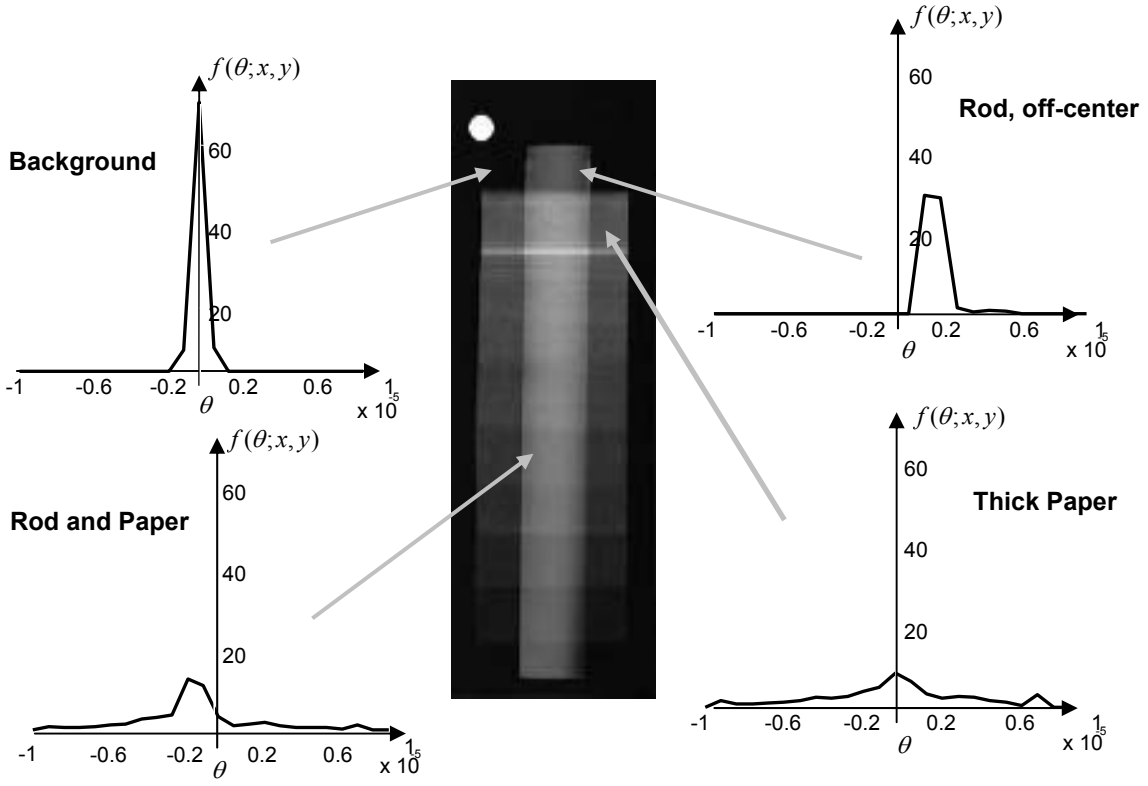

Figure 6. Examples of the deconvolved angular intensity spectrum $f(\theta;x,y)$ as a function of angle, at representative points in the phantom. In the background, the deconvolved curve is a delta function (to within the smoothness imposed by the algorithm). At a pixel off-center in the rod, the curve shows that the beam is deflected to the right, as expected. At a pixel where the rod and paper overlap, the beam is deflected by the rod, and broadened by the paper. At a pixel where there is only paper, the beam is broadened. In every pixel in the object, the beam is also attenuated.

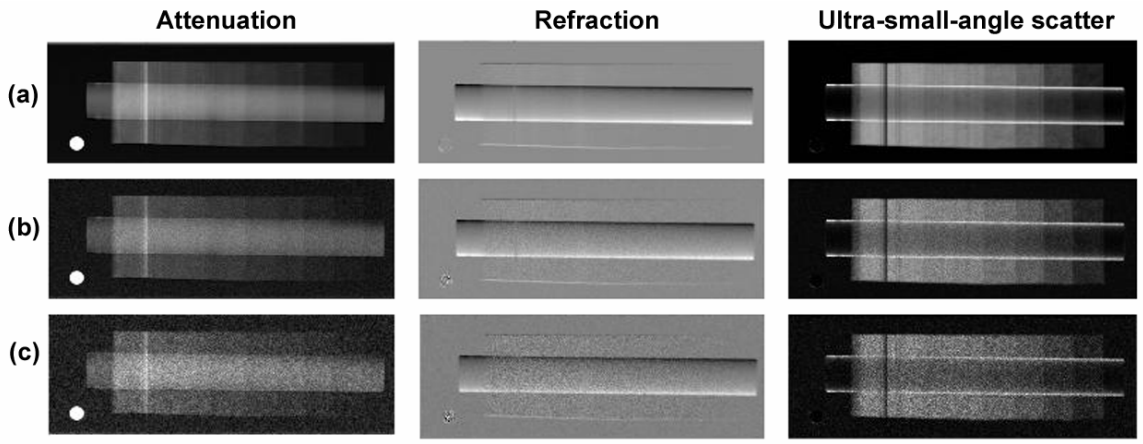

Figure 7. Results of MIR planar-imaging study: (a) images computed from data acquired using a synchrotron; (b) images computed from simulated noisy data, with maximum of 300 ph/pixel; and (c) same as (b), but with maximum counts of 50 ph/pixel. The image quality remains good even at low photon counts.

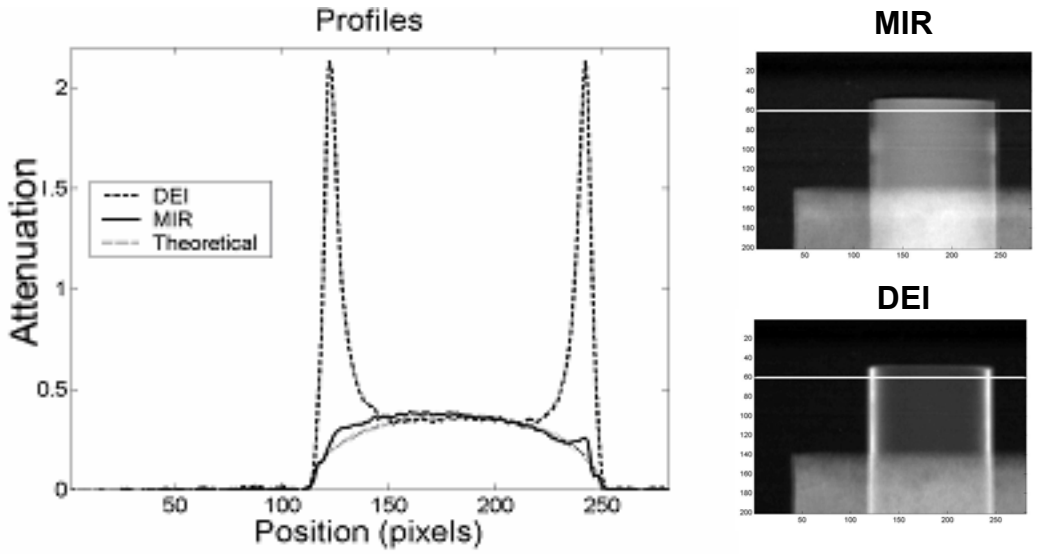

Figure 8. Comparison of MIR and DEI attenuation images. Profiles (left) of the attenuation images (right) show that the DEI image deviates substantially from the theoretical absorption profile of a cylindrical rod, whereas MIR produces a curve that closely approximates it.

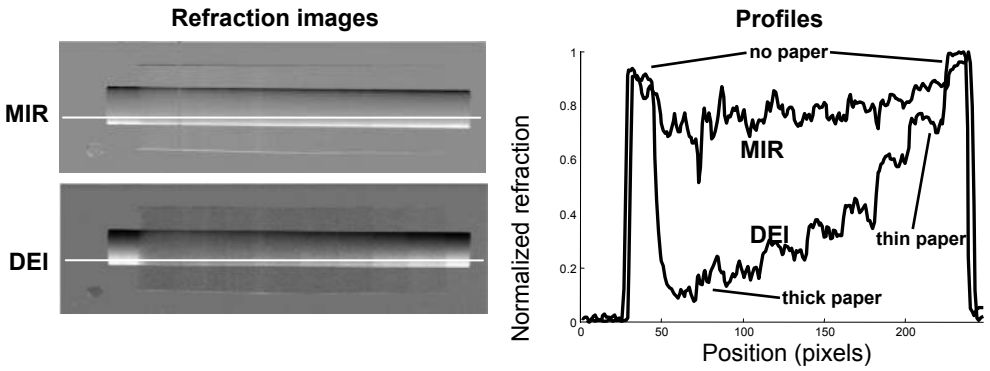

Figure 9. Comparison of MIR and DEI refraction images. One would expect refraction to be constant along the long axis of the rod. Profiles (right) of the refraction images (left) show that the DEI image deviates substantially from a constant, instead showing a staircase pattern caused by contamination from scattering by the paper. The MIR image roughly captures the desired uniform refraction profile, though still exhibits some scatter-induced error.

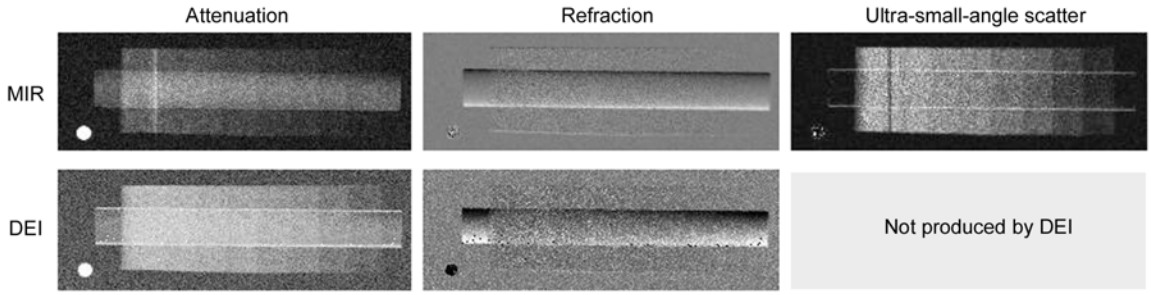

Figure 10. Comparison of MIR and DEI images computed from noisy data.

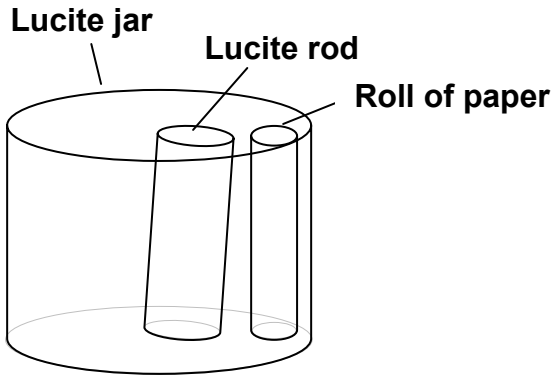

Figure 11. Phantom used in MIR-CT study.

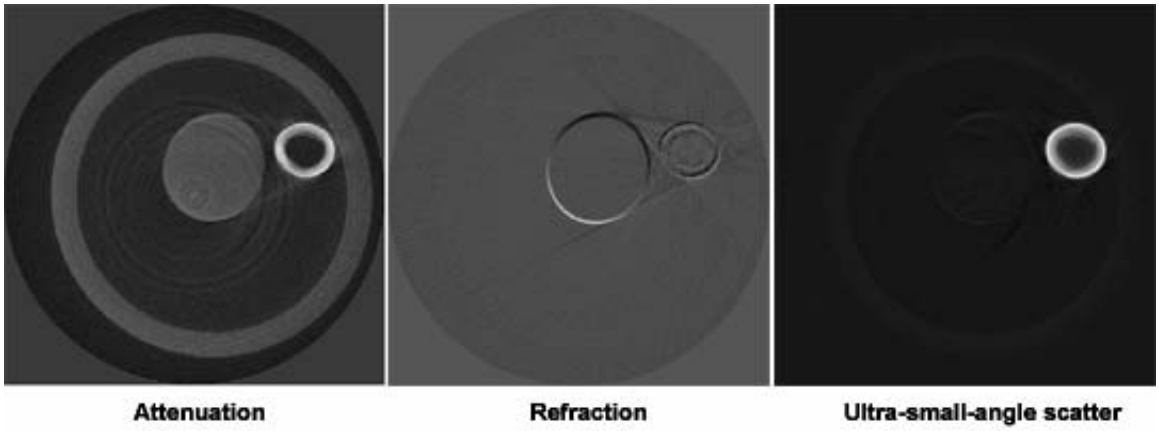

Figure 12. MIR-CT images. As expected, the Lucite rod produces substantial refraction, but little scatter; the converse is true of the paper roll.

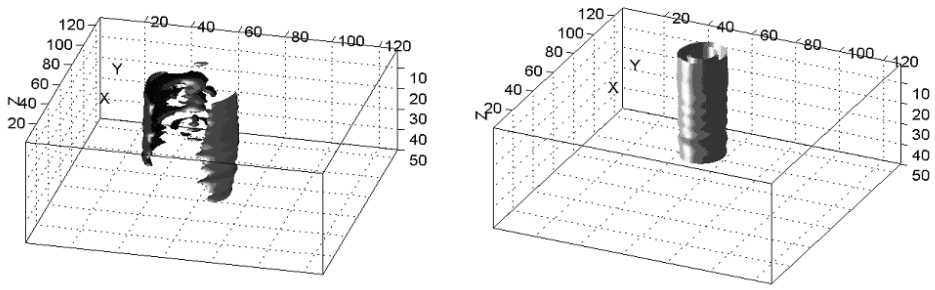

Figure 13. Surface renderings of rod and paper roll in CT phantom. In this simple phantom, paper is easily distinguished by its high values in the scatter image; the surface of the rod is identified by high values at its surface in the refraction image.

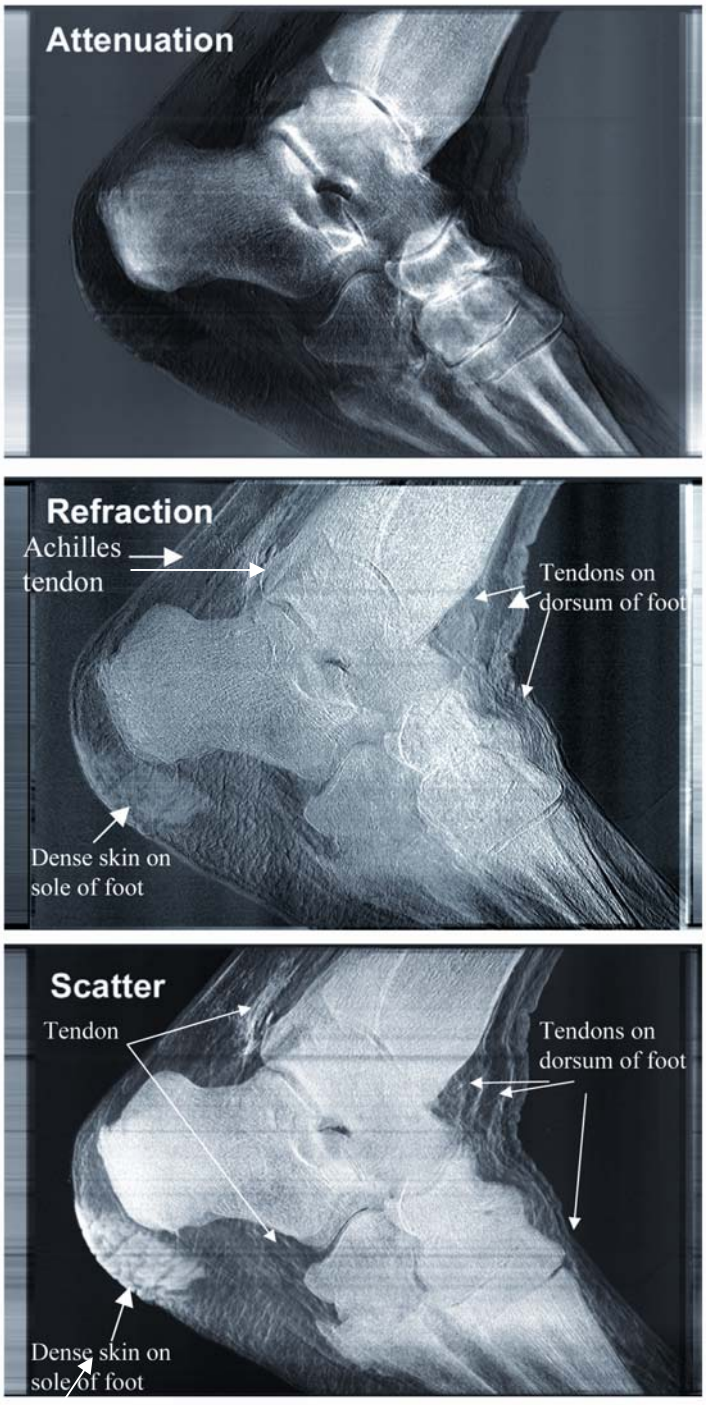

Figure 14. MIR images of a foot: attenuation (top), refraction (middle), and scatter (bottom). Soft tissue features are better visualized in the refraction and scatter images than in the attenuation image.

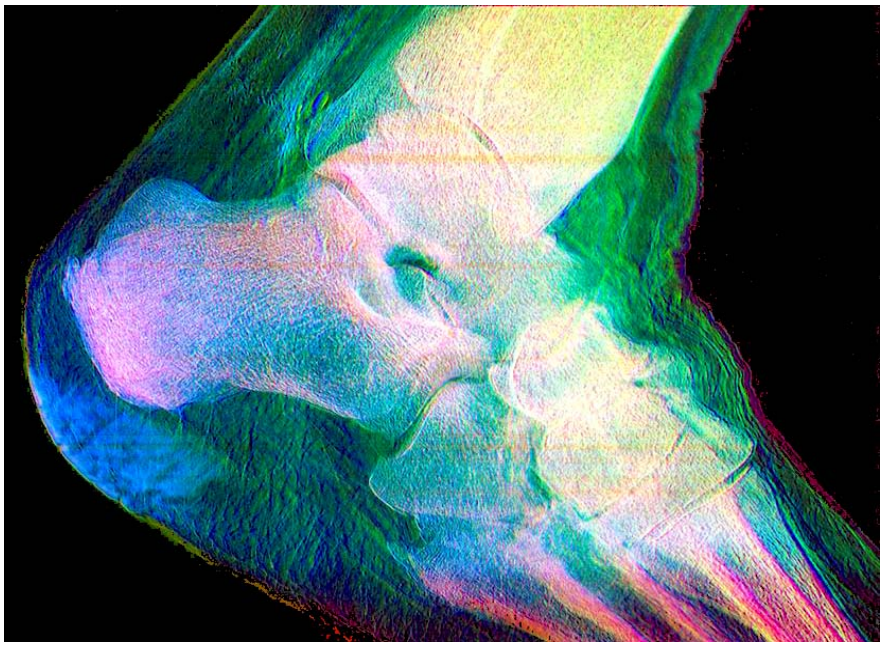

Figure 15. Color-composite MIR image of a foot. Attenuation (red), refraction (green), and scatter (blue) images are shown together in a composite display.

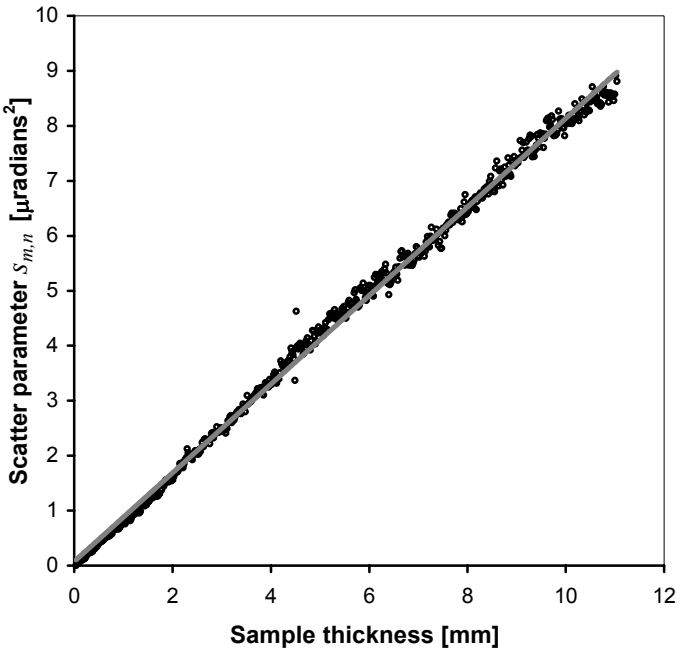

Figure 16. Linearity of MIR scatter parameter with sample thickness. Test object was a wedge-shaped container filled with a suspension of PMMA microspheres in glycerine.